Single entity resolution valving of nanoscopic species in liquids

Eberle, Patric ; Höller, Christian ; Müller, Philipp ; Suomalainen, Maarit ; Greber, Urs F ; Eghlidi, Hadi ; Poulikakos, Dimos

Abstract: Investigating biological and synthetic nanoscopic species in liquids, at the ultimate resolution of single entity, is important in diverse fields. Progress has been made, but significant barriers need to be overcome such as the need for intense fields, the lack of versatility in operating conditions and the limited functionality in solutions of high ionic strength for biological applications. Here, we demonstrate switchable electrokinetic nanovalving able to confine and guide single nano-objects, including macromolecules, with sizes down to around 10 nanometres, in a lab-on-chip environment. The nanovalves are based on spatiotemporal tailoring of the potential energy landscape of nano-objects using an electric field, modulated collaboratively by wall nanotopography and by embedded electrodes in a nanochannel system. We combine nanovalves to isolate single entities from an ensemble, and demonstrate their guiding, confining, releasing and sorting. We show on-demand motion control of single immunoglobulin G molecules, quantum dots, adenoviruses, lipid vesicles, dielectric and metallic particles, suspended in electrolytes with a broad range of ionic strengths, up to biological levels. Such systems can enable nanofluidic, large-scale integration and individual handling of multiple entities in applications ranging from single species characterization and screening to in situ chemical or biochemical synthesis in continuous on-chip processes.

DOI: https://doi.org/10.1038/s41565-018-0150-y

Single entity resolution valving of nanoscopic species in liquids

Patric Eberle[1], Christian Höller[1], Philipp Müller[1], Maarit Suomalainen[2], Urs F. Greber[2], Hadi Eghlidi[1]* and Dimos Poulikakos[1]*

[1]Laboratory of Thermodynamics in Emerging Technologies, ETH Zurich, Sonneggstrasse 3, CH-8092 Zurich, Switzerland

[2] Institute of Molecular Life Sciences, University of Zurich, Winterthurerstrasse 190, CH-8057 Zurich, Switzerland

P.E. and C.H. contributed equally to this work.

*Correspondence to: Hadi Eghlidi (eghlidim@ethz.ch) or Dimos Poulikakos (dpoulikakos@ethz.ch)

Investigating biological and synthetic nanoscopic species in liquids, at the ultimate resolution of single entity, is important in diverse fields[1–5]. Progress has been made[6–10], but significant barriers need to be overcome such as the need for intense fields, the lack of versatility in operating conditions and the limited functionality in solutions of high ionic strength for biological applications. Here we demonstrate switchable electrokinetic nanovalving able to confine and guide single nano-objects, including macromolecules, with sizes down to around 10 nanometers, in a lab-on-chip environment. The nanovalves are based on spatiotemporal tailoring of the potential energy landscape of nano-objects using an electric field, modulated collaboratively by wall nanotopography and by embedded electrodes in a nanochannel system. We combine nanovalves to isolate single entities from an ensemble, and demonstrate their guiding, confining, releasing and sorting. We show on-demand motion control of single immunoglobulin G molecules, quantum dots, adenoviruses, lipid vesicles, dielectric and metallic particles, suspended in electrolytes with a broad range of ionic strengths, up to biological levels. Such systems can enable nanofluidic, large-scale integration and individual handling of multiple entities in applications ranging from single species characterization and screening to in-situ chemical or biochemical synthesis in continuous on-chip processes.

Pneumatic microvalves have enabled microfluidic large scale integration and have significantly advanced lab-on-chip systems and their applications[11–14]. However, the need for much smaller feature sizes and different functioning principles inhibit the direct import of such ideas to the nanoscale and impose new challenges on the way of realizing spatial confinement and controlled guidance of nanoscopic objects in liquids. We introduce the concept of an elektrokinetic nanovalve, which consists of a pair of electrodes placed on either side of a

nanochannel constriction as depicted in Fig. 1a. We combine the function of imposed external electric fields (electrodes) with that of inherent electric double layers in the wall vicinity of nanochannels and selectively fabricated nanotopography, to regulate the potential energy landscape experienced by a nano-object and to non-intrusively control its motion, solely by the configuration of the resulting electric field and forces on the particle. Depending on the voltage applied to the electrodes of the same device, the nanovalve can be operated in both direct current (DC) or alternating current (AC) elektrokinetic modes. While the DC mode can handle particles in low-ionic strength solutions, the AC modes are effective at high ionic strengths. At low ionic strength, the electric double layer of a constriction in the nanochannel acts as an electrostatic barrier that blocks particle passage (closed nanovalve). Applying a DC electric field generates a force that can electrophoretically drive the particle through the constriction (open nanovalve). Conversely, at high ionic strengths, the double layer thickness decreases drastically and the constriction electric field cannot deny the particle passage. The valve is closed by applying an AC field, which stops the particle passage by generating a dielectrophoretic energy barrier and a corresponding "braking" force, holding the particle from going through, shown for up to biological buffer solution ionic concentrations (I≈160 mM)[15]. The nanochannel has a width of 500 nm and a depth of 300 nm; at the constriction the channel becomes shallower with a width of 500 nm and depth of 200 nm (Fig. 1a). Through a communicating microchannel system on the same chip the particles in solution are transported either electrokinetically or with an evaporation-induced flow to the nanochannels (Supplementary Fig. 1). Activating the nanovalve and inducing a favourable potential energy landscape moves the particles in the surrounding liquid. Figures 1b,c,d,e illustrate the functional principle of the valve on a single gold nanoparticle (100 nm in diameter) and an adenovirus particle (~90 nm in diameter), in solutions

with ion concentrations spanning almost three orders of magnitude, respectively[16]. The in-plane trajectories of the particles are overlaid on the scanning electron micrograph (SEM) of the valve for clarity. The trajectories of all nanoscale species studied in this work were obtained with either fluorescence or interferometric scattering (iSCAT)[17]. In frame (I) (Fig. 1b,c) the particle is prevented from passing through the closed valve due to the presence of a potential energy barrier, while in frame (II) an externally controlled change in the potential energy landscape induced by the electrode voltages, opens the valve and enables the particle to move through.

The potential energy landscape is generated by electrostatic and dielectrophoretic interactions. When exposed to water, the SiO_2 channel walls attain a double layer with a decaying electrostatic potential of a characteristic Debye length $\kappa^{-1} \propto 1/\sqrt{I}$ [18,19]. For low ionic strength electrolytes ($I < 0.5$ mM) the Debye length κ^{-1} is several tens of nm long[20,21] and, the double layers from a charged nano-object and the channel wall can interact leading to a potential energy landscape[9,22]. At the channel constriction, because of increased interaction, a potential energy barrier ΔU_P for the particle is formed. This barrier can be substantially higher than the inherent thermal energy $k_B T$ (k_B, Boltzman constant) of the nano-object (Fig. 1d, orange curve), and can prevent its passage over the barrier (closed valve)[9,23]. A sufficiently large DC electric field by applying a voltage between the two nanoelectrodes reduces the barrier such that it is overcome by the energy of the particle, which advances itself forward (open nanovalve).

The DC mode fails for electrolytic strengths, I, larger than ~0.5 mM due to the reduced thicknesses of the double layers (to few nm)[19,20]. Most biological solutions have ionic strengths of the order of ~150 mM[15], more than two orders of magnitude higher than this limit.

The principle of the AC mode is based on dielectrophoretic forces, which can readily extend the functionality of the device into the realm of biologically relevant solutions. The time-averaged potential energy in this case is $\langle U \rangle = -2\pi\varepsilon_m R^3 \,\mathrm{Re}(CM)\left|\mathbf{E}_{AC}\right|^2$, where ε_m, R, Re(CM) and $\mathbf{E}_{AC}$ are the electrolyte permittivity, the effective particle radius, the real part of the Clausius-Mossotti (CM) factor and the root-mean-square (rms) electric field from the applied AC voltage, respectively[18,24]. Re(CM) is a function of the conductivities and permittivities of the particle and electrolyte and varies with frequency [18,24]. For negative values of Re(CM) we can obtain a potential energy barrier within the constriction due to the corresponding increase of the electric field, $\mathbf{E}_{AC}$.

The simulated potential energy profiles in Fig. 1e show that for a sufficiently high AC voltage (green and orange curves) the particle experiences a potential energy barrier substantially higher than its thermal energy and is prevented from going through the constriction (closed valve)[23]. In contrast, for V_{AC} = 0 V (blue curve) the potential energy barrier is not present and the particle can move through the constriction (open valve).

Connecting two such nanovalves in series allows us to guide a particle to the interspace between the two nanovalves, confine it and release it on-demand (Fig. 2a). In such a trap-in-channel, the central electrode (C) is shared by the two nanovalves. In Fig. 2a and in Supplementary Video 1 we demonstrate guiding, confining and releasing of an adenovirus in buffer solution (0.2X PBS, $I \approx 32$ mM) in AC mode. Furthermore, we employed the AC mode to handle a 100-nm (diameter) lipid vesicles (Supplementary Fig. 2), and the DC mode to handle a 100-nm spherical gold nanoparticle (Supplementary Video 2 and Supplementary Fig. 3a) in a trap-in-channel structure.

The potential energy barrier in the AC mode ΔU_P ($\propto R^3 |\mathbf{E}_{AC}|^2$) rapidly decreases as the particle size (R) decreases. However, $|\mathbf{E}_{AC}|^2$ scales with $1/L^4$, where L is the characteristic cross-sectional dimension of the channel constriction. Therefore, the drop of the potential energy barrier for very small nano-objects can be compensated by shrinking the cross-section of the channel constriction. For the valves in Fig. 2b and 2c we reduced the cross-section of the constriction to 70 x 70 nm^2 (Supplementary Fig. 4 shows the design). The nanotopography of this nanovalve, allows us to perform valving of particles down to single macromolecules. The configuration shown employs three joined and independently operated nanovalves, in a Y-junction. Such a trap-in-junction device can be used to isolate, sort, mix (or combine) individual nano-objects from an ensemble of nano-objects at the nanochannel entrance entering the nanochannel serially. Figure 2b demonstrates the capabilities of this system to isolate a single quantum dot (QD 625 ITK Carboxyl, Thermo Fischer Scientific, 10 x 12 nm^2) from an ensemble in the junction (centre), confine it there and release it on demand to the top-left (left panel) or to the top-right (right panel) channel (sorting, see also Supplementary Video 3). The left sequence also demonstrates that particles can be independently controlled: while the isolated QD is confined and guided to the left, another QD of the ensemble is prevented from entering the trap by the closed valve. Fig. 2c and Supplementary Video 4 show a similar motion control and valving of a single immunoglobulin G molecule (Goat anti-Rabbit IgG, tagged with Alexa Fluor Plus 488, Thermo Fisher Scientific, 144 kDa). Single molecules are first isolated in the trap and subsequently released to the top-left (left panel) or top-right (right panel) nanochannels. While tracing the molecules in the micro- and nanochannel is difficult due to their very fast and large thermal fluctuations, they become easily traceable in the trap when their motion is confined. This

may enable studies of their optical contrast, for example for mass spectroscopy[25] and statistical motion, determining their various properties, such as charge[22], dielectric properties and polarizability. In Supplementary Fig. 5 and Supplementary Video 5, the same sequence in the trap-in-junction device is shown for an adenovirus. Furthermore, we used the DC mode to control the motion of a 100-nm (Supplementary Video 6) and a 60-nm (Supplementary Fig. 3b) gold particle. Supplementary Video 7 shows a sequence for simultaneous control of two 100-nm polystyrene beads in AC mode (0.1X PBS, $I \approx 16$ mM) and two 100-nm gold particles in DC mode ($I = 0.05$ mM), enabling the study of their interactions.

To investigate the probability distribution of the lateral particle displacement and potential energy in a nanovalve, we recorded the position of a trapped 100-nm fluorescent polystyrene bead (Fig. 3a). The right diagram shows the particle probability density and potential energy profile (dots) calculated from the scatter plot and corrected for the finite exposure time[26]. Electric field distribution is obtained using Finite Element Method (FEM). The results are substituted into the Boltzmann probability distribution (equation 9, Methods) and fitted to the measured probability distribution p(r) using Re(CM) as a fitting parameter (see Methods, Section AC mode). The mean lateral displacement along the channel increases when going from 0.1X to 1X PBS concentration. This can be explained by the lower CM-factor and the weakening of the electric field in the valve at 1X PBS concentration, originating from the enhanced screening of the charges at the electrodes. From these fitted simulations we obtained $\Delta U_P \approx 17 k_B T$ and $\Delta U_P \approx 10 k_B T$ for the 0.1X PBS and 1X PBS cases, respectively. These values of the potential energy barriers can be independently calculated by inserting the measured residence times of the trapped particles into Kramer's relation[23,27]. For the 0.1X PBS and 1X PBS concentrations, we repeatedly measured residence times of the order of several tens of minutes and tens of seconds,

146 respectively. These values correspond to potential energy barriers, in good agreement with the
147 fitted simulations mentioned above. In Fig. 3b we present the measurements of an adenovirus
148 and observe an increase in the confinement, when going from V_{AC} = 1.75 V to V_{AC} = 2.25 V. This
149 is the result of an increase in the potential energy barrier (proportional to $|\mathbf{E}_{AC}|^2$, equation 8,
150 Methods) for higher applied voltages. The residence times for V_{AC} = 1.75 V and V_{AC} = 2.25 V
151 were of the order of several tens of seconds and several minutes, respectively. Using Kramer's
152 law we estimate $\Delta U_P \approx 10 k_B T$ and $\Delta U_P \approx 13 k_B T$ for the two cases.

153 Figure 4 summarizes the broad range of cases demonstrated with our nanovalving platform.
154 These include handling of biological and artificial nanoscopic entities with varying sizes and
155 surface charges under a broad range of electrolytic strengths. The operational range for the DC is
156 limited to I < ~0.5 mM and highly charged particles. In contrast, the AC mode is capable of
157 handling a diverse range of nano-objects in electrolytes of ionic strengths up to physiological
158 conditions, $I \approx$ 160 mM. The cross-sectional dimensions of the smallest channel constriction
159 made possible valving of particles down to QDs (~10 nm) and single macromolecules[28].
160 Although there is no intrinsic limitation regarding further downsizing toward particle sizes O(1
161 nm) in the involved physics and fabrication, there are limitations in detection and tracing of
162 small molecules, which normally generate low optical contrast, and undergo photobleaching (in
163 fluorescence) and very fast thermal diffusion (inversely proportional to the molecule size).

164 In closing, we introduced in this work the concept and actual device of an electrokinetic
165 nanovalve. The nanovalve exploits different physical principles (electrophoresis,
166 dielectrophoresis and electrostatic trapping) working collaboratively with nanotopography in a
167 nanochannel. The variability of the amplitude and frequency of the applied voltages and the

ability to operate in two different modes (AC and DC) enable the control of a great variety of particle types in a large range of ionic concentrations up to biological levels (Fig. 4). Such nanovalves can be potentially combined to construct systems of chip-based nanofluidic devices, two basic cases of which (with combining 2 and 3 nanovalves) we have demonstrated.

Note added in proof

During the review process of this work, another independent experimental work appeared, by Skaug et al.[29], in which, electrostatic effects (similar to the DC mode presented here) in combination with DC fields generated by electrodes, was used to move charged metallic particle ensembles of two mixed sizes (60 nm and 100 nm) and rapidly sort them into two subsets of these two sizes at low salt concentration (less than 1 mM).

References

1. Greber, U. F. & Way, M. A Superhighway to Virus Infection. *Cell* **124,** 741–754 (2006).

2. Pang, Y., Song, H., Kim, J. H., Hou, X. & Cheng, W. Optical trapping of individual human immunodeficiency viruses in culture fluid reveals heterogeneity with single-molecule resolution. *Nat. Nanotechnol.* **9,** 624–630 (2014).

3. Amstad, E. & Reimhult, E. Nanoparticle actuated hollow drug delivery vehicles. *Nanomedicine* **7,** 145–164 (2012).

4. Aguilar, C. a & Craighead, H. G. Micro- and nanoscale devices for the investigation of epigenetics and chromatin dynamics. *Nat. Nanotechnol.* **8,** 709–18 (2013).

5. Neuman, K. C. & Nagy, A. Single-molecule force spectroscopy: optical tweezers, magnetic tweezers and atomic force microscopy. *Nat. Methods* **5,** 491–505 (2008).

6. Grier, D. G. A revolution in optical manipulation. *Nature* **424,** 810–816 (2003).

7. Berthelot, J. *et al.* Three-dimensional manipulation with scanning near-field optical nanotweezers. *Nat. Nanotechnol.* **9,** 295–299 (2014).

8. Fields, A. P. & Cohen, A. E. Electrokinetic trapping at the one nanometer limit. *Proc. Natl. Acad. Sci. U. S. A.* **108,** 8937–8942 (2011).

9. Krishnan, M., Mojarad, N., Kukura, P. & Sandoghdar, V. Geometry-induced electrostatic trapping of nanometric objects in a fluid. *Nature* **467,** 692–695 (2010).

10. Ding, X. *et al.* On-chip manipulation of single microparticles, cells, and organisms using surface acoustic waves. *Proc. Natl. Acad. Sci. U. S. A.* **109,** 11105–11109 (2012).

11. Unger, M. a, Chou, H. P., Thorsen, T., Scherer, a & Quake, S. R. Monolithic

microfabricated valves and pumps by multilayer soft lithography. *Science* **288,** 113–116 (2000).

12. Thorsen, T., Maerkl, S. J. & Quake, S. R. Microfluidic Large-Scale Integration. *Science* **298,** 580–584 (2002).

13. Neuži, P., Giselbrecht, S., Länge, K., Huang, T. J. & Manz, A. Revisiting lab-on-a-chip technology for drug discovery. *Nat. Rev. Drug Discov.* **11,** 620–632 (2012).

14. Valencia, P. M., Farokhzad, O. C., Karnik, R. & Langer, R. Microfluidic technologies for accelerating the clinical translation of nanoparticles. *Nat. Nanotechnol.* **7,** 623–629 (2012).

15. Williams, R. J. P. & Frausto da Silva, J. J. R. *The natural selection of the chemical elements: the environment and life's chemistry*. (Clarendon Press, 1996).

16. Reddy, V. S., Natchiar, S. K., Stewart, P. L. & Nemerow, G. R. Crystal structure of human adenovirus at 3.5 A resolution. *Science* **329,** 1071–1075 (2010).

17. Kukura, P. *et al.* High-speed nanoscopic tracking of the position and orientation of a single virus. *Nat. Methods* **6,** 923–927 (2009).

18. Morgan, H. & Green, N. G. *AC Electrokinetics: Colloids and Nanoparticles*. (Research Studies Press, 2003).

19. Duan, C. & Majumdar, A. Anomalous ion transport in 2-nm hydrophilic nanochannels. *Nat. Nanotechnol.* **5,** 848–852 (2010).

20. Sparreboom, W., van den Berg, A. & Eijkel, J. C. T. Principles and applications of nanofluidic transport. *Nat. Nanotechnol.* **4,** 713–720 (2009).

21. Tae Kim, J., Spindler, S. & Sandoghdar, V. Scanning-aperture trapping and manipulation of single charged nanoparticles. *Nat. Commun.* **5,** 3380 (2014).

22. Ruggeri, F. *et al.* Single-molecule electrometry. *Nat. Nanotechnol.* **12,** 488–495 (2017).

23. Kramers, H. a. Brownian motion in a field of force and the diffusion model of chemical reactions. *Physica* **7,** 284–304 (1940).

24. Pethig, R. Dielectrophoresis: Status of the theory, technology, and applications. *Biomicrofluidics* **4,** (2010).

25. Young, G. *et al.* Quantitative mass imaging of single molecules in solution. *bioRxiv* (2017). at <http://biorxiv.org/content/early/2017/12/06/229740.abstract>

26. Savin, T. & Doyle, P. S. Role of a finite exposure time on measuring an elastic modulus using microrheology. *Phys. Rev. E - Stat. Nonlinear, Soft Matter Phys.* **71,** 6–11 (2005).

27. Libchaber, A. & Simon, A. Escape and Synchronization of a Brownian Particle. *Phys. Rev. Lett.* **68,** 3375–3378 (1992).

28. Goldsmith, R. H. & Moerner, W. E. Watching conformational- and photodynamics of single fluorescent proteins in solution. *Nat. Chem.* **2,** 179–186 (2010).

29. Skaug, M. J., Schwemmer, C., Fringes, S., Rawlings, C. D. & Knoll, A. W. Nanofluidic rocking Brownian motors. *Science* **359,** 1505–1508 (2018).

Acknowledgements

We appreciate the support from Binnig Rohrer Nanotechnology Center of ETH Zurich and IBM Zurich. We thank Manish K. Tiwari for his support in the very beginning phase of work related to trapping of nanoscale matter in channels; Yuriy Federoshyn for EBL exposures, Helge Ewers for providing the lipid vesicle solutions; Francesco Robotti, Simone Bottan, Martin Bergert, Costanza Giampietro, and Aldo Ferrari for help with biological species; Julian Marschewski for electrode characterization; Alois Renn and Thomas Schutzius for fruitful discussions; and Jovo Vidic for technical support. We acknowledge the help of Moritz Wöhrwag and Pascal Gschwend, for performing some analysis at the early stage of the project, and the Particle Technology Laboratory (PTL) at ETH Zurich for providing access to their zetasizer instrument. The work was partially supported by the Swiss National Science Foundation under Grant Nr. 200021_162855and Grant Nr. 310030B_160316.

Author contributions

P.E., H.E. and D.P. conceived the research, designed the experiments, analyzed data and wrote the manuscript. P.E. designed and fabricated the devices, and performed theoretical analysis. H.E. designed and implemented the optical imaging systems. P.E., C.H. and P.M. performed experiments. M.S. and U.G. provided adenoviruses and expertise on viral particles. H.E. and D.P. supervised all aspects of the project. All authors proofread the manuscript.

Competing interests

The authors declare no competing financial interests.

Additional information

Supplementary information is available in the online version of the paper. Reprints and permission information are available online at www.nature.com/reprints. Correspondence and requests for materials should be addressed to H. Eghlidi or D. Poulikakos.

Data availability

The data that support the plots within this paper and other findings of this study are available from the corresponding authors upon reasonable request.

Supplementary information

Supplementary Text, Supplementary Figures 1–13, Supplementary Video Captions 1-7, Supplementary References

Figure 1. Concept and use of electrokinetic nanovalves. a, Illustration of the electrokinetic nanovalve composed of two nanoelectrodes (yellow) placed on either side of the channel constriction and the schematic of an adenovirus. **b,** A gold nanoparticle (100 nm in diameter, surface charge: ~–150*e*) in liquid with low ionic strength (I = 0.05 mM) handled with DC mode. Frame (I): particle is prevented from going through the valve by the potential energy barrier (closed state); frame (II): upon removing the potential energy barrier the particle passes through the valve (open state). **c,** Adenovirus (~90 nm in diameter) in liquid with high ionic strength (0.2X PBS: $I \approx 32$ mM) handled with AC mode. In frame (I) the valve is closed and in frame (II) the valve is open. (b and c) Left side electrodes were placed away from the constriction and are not visible in the image. Trajectories are overlaid on an SEM image of the nanovalve. **d,** Potential energy of the gold particle (100 nm in diameter) in (b) for closed (orange) and open (blue) states. Open state: $\mathbf{E}_{DC} = -12$ mV/μm bends potential profile, decreases barrier ($\Delta U_P \approx 17 k_B T \rightarrow \sim k_B T$) and actuates nanoparticle. **e,** Potential energy of a polystyrene bead (100 nm in diameter, $\mathrm{Re}(CM) \approx -0.18$) in 0.1X PBS ($I \approx 16$ mM) for closed (green $\mathbf{E}_{AC}$ = 625 mV/μm, orange $\mathbf{E}_{AC}$ = 850 mV/μm) and open (blue, $\mathbf{E}_{AC}$ = 0 mV/μm) states. All electric fields are specified at the constriction. Dimensions of the device are h = 300 nm, g = 180 – 220 nm, s = 500 nm, p = 400 nm and w = 500 nm. Scale bars show 500 nm.

Figure 2. Guiding, confining and releasing adenoviruses, quantum dots and immunoglobulin G antibodies. a, An adenovirus guided in AC mode within a trap-in-channel in 0.2X PBS ($I \approx 32$ mM, $V_{AC} = 1.75$ V, $\mathbf{E}_{AC} \approx 800$ mV/μm). Adenovirus is (I) prevented from going through the left nanovalve (left potential barrier present), (II) moves through the left nanovalve (left potential barrier removed), (III) is confined within the valves interspace (left potential barrier restored) and (IV) moves through the right nanovalve (right potential barrier removed). Potential energy profiles for the nano-object obtained from numerical simulations are shown for each step. **b,** On-demand isolating from an ensemble, confining and sorting of single quantum dots (~ 10 nm in diameter) to the left (sequences I-IV) or right (sequences V-VIII) channels in trap-in-junction by switching potential barriers ($V_{AC} = 2$ V, $\mathbf{E}_{AC} \approx 900$ mV/μm) on and off in AC mode in 0.1X borate-buffered saline ($I \approx 16$ mM). The left sequence shows that the trapped QD (trajectory shown with orange dots) can be isolated and manipulated independently from another quantum dot (trajectory shown with red dots) of the ensemble, which is prevented from entering the trap by the closed lower valve. Dimensions of the channel at the bow-tie structure, on top of the step constriction, are g = 40 nm and o = 70 nm. (a and b) Time-trace diagrams show electrode voltages for each step. **c**, On-demand isolation, confinement and sorting of single immunoglobulin G antibodies (144 kDa) to the left (sequences I-IV) or right (sequences V-VIII) channels in a trap-in-junction device in AC mode in 0.1X PBS ($I \approx 16$ mM). (a, b and c) Trajectories are overlaid on top of SEM images. Scale bars show 500 nm.

Figure 3. Lateral displacement of polystyrene bead and adenovirus in AC mode. Scatter plots of lateral (x-y) positions and probability density $p(x)$. **a,** A 100-nm (diameter) fluorescent polystyrene bead in 0.1X PBS solution at V_{AC} = 2.0 V ($\mathbf{E}_{AC} \approx$ 900 mV/μm, orange), and in 1X PBS solution at V_{AC} = 3.0 V ($\mathbf{E}_{AC} \approx$ 800 mV/μm, blue) measured at 200 fps in a trap-in-channel structure. The solid lines and dots show the simulation and experimental results, respectively. **b,** Adenovirus in 0.2X PBS solution at V_{AC} = 1.75 V ($\mathbf{E}_{AC} \approx$ 800 mV/μm, blue) and V_{AC} = 2.25 V ($\mathbf{E}_{AC} \approx$ 1000 mV/μm, orange) measured at 28 fps in a trap-in-channel structure. Probability density $p(x)$ and potential energy $U_P(x)$ obtained from the scatter plots (dots) and simulation (solid lines) fitted to measurements using the *CM*-factor as a fitting parameter. $U_P(x)$ is corrected for the finite exposure time (see Supplementary Table 1). Scale bars show 500 nm.

Figure 4. Investigated nanoscale species and corresponding conditions. A broad selection of nano-object types and immunoglobulin G antibodies with different particle zeta potentials ψ, successfully controlled in liquids with markedly different electrolyte ionic strengths *I,* spanning more than three orders of magnitude. Operational range of DC mode for a 100-nm particle (surface charge: ~–150*e*) is shown in orange. Crossing the DC mode boundary (curved black dashed line, corresponding to $\Delta U_P \approx 7.5 k_B T$) from left to the right (*I* increasing) the topographically induced potential energy barrier gradually vanishes. In the AC mode (operational range shown in blue) the nanovalve can be operated at higher ionic strengths and also when surface-passivation agents are employed. DC mode fails for both these conditions. For lipid vesicles, immunoglobulin G antibodies and adenoviruses the channel-walls were passivated with Bovine Serum Albumin (BSA) and Polyethylene Glycol (PEG) to avoid sticking.

Methods

Preparation of biological and synthetic particles

Gold nanoparticles (60 and 100 nm in diameter, British Biocell International), gold nanorods (50 nm x 95 nm, Nanopartz) and fluorescent carboxylate modified polystyrene beads (40 nm and 100 nm in diameter, FluoSpheres 505/515, ThermoFischer Scientific) were washed by centrifugation (800 g, 5 minutes) and redispersed in deionized (DI) water (> 18 MΩcm) to reduce ionic strength of solution and remove contaminants (gold particles required three and PS beads required one washing cycle). KCl was used to adjust the ionic strength of the particle solution. Solutions of fluorescent beads were also redispersed in 0.1X and 1X PBS. Solution of quantum dots (~10 x 12 nm^2, Qdot 625 ITK Carboaxyl, ThermoFischer Scientific) was diluted 1:100 in borate buffered saline (BBS) to 0.2X and 1X buffer concentration. Solution of immunoglobulin G antibodies (IgG, Goat anti-Rabbit IgG, Alexa Fluor Plus 488, Thermo Fisher Scientific, catalog number A32731, 144 kDa) was diluted to 1:20000 in 0.1X PBS concentration with the addition of 5% Bovine Serum Albumin (BSA).

Lipid vesicles (~100 nm in diameter) prepared by extrusion and tagged with Atto 532 fluorophores by covalent attachment were dialyzed and diluted in DI water (> 18 MΩcm). Lipid vesicles were also redispersed in PBS solution of 0.1X and 1X concentration.

Solution of adenoviruses, HAdV-C2_TS1, (~90 nm in diameter) was purified twice over caesium chloride gradient and dialyzed against 0.1 M sodium bicarbonate-50 mM NaCl-1 mM $MgCl_2$ and was reacted with Alexa Fluor 488 5-TFP amine reactive dye (Thermo Fisher Scientific) for 1 hour at room temperature in dark[30]. Unincorporated dye was removed by banding the virus on

caesium chloride gradient, and subsequently the virus was dialyzed against storage buffer (10 mM Tris-HCl pH 8.1-150 mM NaCl-1 mM $MgCl_2$).

Solution of labeled adenoviruses was diluted in PBS to 0.2X and 1X buffer concentration with the addition of 0.02 Vol% Tween 20. The handlings of the viruses, including loading them into nanochannel chips and cuvettes for zeta potential measurements, sealing the loaded devices, and autoclaving of the used devices, were carefully performed in a biosafety level 2 classified biolab.

Infection assay: A549 (human lung epithelial carcinoma) cells were seeded at a density of 6000 cells per well in a 96-well imaging plate in A549 growth medium (DMEM supplemented with 7.5 % fetal calf serum and 1% nonessential amino acids) and grown over two nights. HAdV-C5_EGFP virus, a non-replicating reporter virus expressing the enhanced green fluorescent protein (EGFP)[31,32] was preincubated in PBS/0.02% Tween 20 or 0.2xPBS/0.02% Tween 20 for 5 hours at room temperature, and then diluted into the A549 growth medium for infection. The infected cells were analyzed after 24 hours post infection as described in reference[33]. The average intensity of the EGFP signal over a nuclear area (DAPI stain) was taken as a measure of infection efficiency. The infectivity of the HAdV-C5 was retained in the above specified assay buffers (Supplementary Fig. 6).

Zeta potentials and conductivities of the particle solutions were measured by means of dynamic light scattering in a Malvern Zetasizer. The ionic strengths of particle solutions with low ionic strengths (non-buffered) were determined by conductivity measurements and assuming symmetric monovalent electrolytes[18]. For particle solutions with high ionic strengths (buffered), the ionic strengths were determined by the concentrations of the buffer solutions.

368 Interferometric scattering (iSCAT) and fluorescence microscopy

369 Gold nanoparticles and nanorods were imaged by the interferometric scattering (iSCAT)
370 technique[17,34] at 1000 fps acquisition rate in a home-built inverted microscope equipped with
371 high numerical aperture (1.3 NA) objective, a diode pumped green laser (532 nm) for excitation,
372 and a CMOS camera (MV-1024-160-CL, PhotonFocus) for imaging (Supplementary Fig. 7a).
373 Fluorescent particles, lipid vesicles, viruses, QDs and IgG molecules were imaged in a home-
374 built inverted microscope setup equipped with a 450 nm laser (for exciting fluorescent beads,
375 viruses, QDs and IgG molecules) and a 532 nm laser (for exciting lipid vesicles). The
376 fluorescence signal was collected by a 100X, 1.4 NA objective and measured by a scientific
377 CMOS camera (Andor Zyla 4.2 sCMOS), for fluorescent beads, lipid vesicles and viruses, or an
378 EMCCD (iXon Ultra 888) for QDs and IgG molecules. QDs and IgG molecules have low
379 emission intensities and tracking their fast motion requires cutting-edge high-sensitivity cameras
380 (such as EMCCD) and a careful optimization of the optical system. Long-pass filters (cut-off at
381 500 nm for 450 nm excitation and 550 nm for 532 nm excitation) were used in the detection path
382 to remove the excitation light (Supplementary Fig. 7b). In the presented single molecule
383 measurements (Fig. 2c and Supplementary Video 4), to increase the contrast and reduce the dark
384 noise, we have subtracted the background (averaged over 100 frames) and used a median filter.

385 Filling and loading of the chip

386 First, the chip was filled with the electrolyte used in the experiment. The liquid in fluidic port P1
387 (Supplementary Fig. 1a) was removed by pipetting it out and then replaced by an equal amount
388 of nanoparticle solution. For the adenovirus, this step was performed in a biosafety classified

level 2 lab and the open ports of the chip were closed and firmly sealed. The exterior was disinfected before the chip was transferred to the experimental setup.

For the DC mode (low ionic strength), the particles were driven into the microchannel by an evaporation induced flow from port P1 to P2 or/and by an electric field induced by an externally applied voltage on the electrodes E_{P1} and E_{P2} (Supplementary Fig. 1a). Within the nanochannels the particles were moved by an electric field induced by applying an external voltage on the nanoelectrodes (E_{nano}) or on the microchannel-electrodes ($E_{\mu 1}$ and $E_{\mu 2}$) (Supplementary Fig. 1a,b).

For the AC mode (high ionic strength), the particles were driven into the microchannel by an evaporation induced flow from port P1 to P2 (Supplementary Fig. 1a) or/and by diffusion. Within the nanochannels the particle motion was based on diffusion.

Fabrication process of the device

The fabrication process included additive (depositions), subtractive (etchings) and pattern transfer techniques such as electron-beam lithography (EBL, Vistec 100kV system) and photolithography (PL, Karl Süss mask aligner MA/BA6). The result of each fabrication step was characterized by optical microscopy, scanning electron microscopy (SEM), profilometry, and when required, atomic force microscopy (AFM) and ellipsometry. The process steps are schematically shown and explained in detail in Supplementary Fig. 8. Scanning electron micrographs of fabricated trap-in-channel and trap-in-junction structures are shown in Supplementary Fig. 1b. The design and electrochemical characterization of nanoelectrodes can be found in the Supplementary Text and Supplementary Fig. 9.

Residence time and position probability density of the particle in a potential energy well

A particle can be confined in a potential energy well (minimum). The mean residence time, i.e. the mean time before the particle escapes, can be estimated by Kramer's law[23,27]

$$\tau = \tau_R \exp\left(\Delta U_P / k_B T\right), \tag{1}$$

where τ_R is the characteristic relaxation time as defined in the previous section, and ΔU_P is the potential barrier height or depth of the potential energy well.

The probability density distribution $p(\mathbf{r})$ of the position of the particle in the well with potential energy function $U_P(\mathbf{r})$ can be obtained by the Boltzmann distribution according to[35]

$$p(\mathbf{r}) = \frac{\exp\left(\dfrac{-U_P(\mathbf{r})}{k_B T}\right)}{\dfrac{1}{V}\int_V \exp\left(\dfrac{-U_P(\mathbf{r})}{k_B T}\right)\left|d\mathbf{r}\right|}, \tag{2}$$

where $\mathbf{r}$ and V denote the centre of mass position of the particle and the volume of the nanovalve, respectively, and $\frac{1}{V}\int_V p(\mathbf{r})\left|d\mathbf{r}\right| = 1$.

DC mode

In the DC mode, the double layers at the particle and the channel walls interact. For the case of no applied voltage the potential energy of the particle is equal to the change in free energy in the electrolyte ($U_P = F$, see Supplementary Text)[36,37]. The electric free energy potential (F) can be written in the following form[36,37]

$$F = U_{el} - T\Delta S\,. \tag{3}$$

427 U_{el} is the electrostatic energy and ΔS is the entropy difference due to redistribution of ions in the
428 presence of charged objects[36,37].

429 The electrostatic potential (φ) and charge distribution in an electrolyte can be obtained by solving
430 the Poisson-Boltzmann equation with the relevant boundary conditions[37]. To minimize the free
431 energy, counter-ions screen a charged surface by building up a double layer comprising a thin
432 and compact Stern layer of relatively immobile ions closely bound to the surface and a diffusive
433 layer of mobile ions extending into the electrolyte[18]. The characteristic length (Debye length, see
434 main text) of the diffusive part of the double layer can be interpreted as the electrostatic
435 interaction length[18]. For the case of applied potential, the potential energy (U_P) of the particle can
436 be written as the sum of two terms: the electric free energy (F) which considers the contributions
437 from the charge distribution and its associated electrostatic potential, and the electric field along
438 the channel induced by the externally applied DC voltage (equation (4) below). We solved the
439 Poisson-Boltzmann equation to obtain the ion distribution in the electrolyte and assumed
440 constant surface charge densities on the SiO_2 channel walls and on the particle surface as
441 boundary conditions[9]. For the SiO_2 channel walls, a surface charge density $q_s = -1.6$ mC/m^2 was
442 used[9,38]. At the nanoelectrodes, the surface charge density was set to zero. For the particles, we
443 employed an approximate equation to calculate the surface charges from the measured zeta
444 potentials[9]. Due to the interacting double layers the effective surface charge densities are smaller
445 and are a function of the Debye length and the separation of particle and channel walls[38]. In our
446 simulations we accounted for this by employing a reduction factor according to reference[38], for
447 the surface charge densities of the channel walls and the particle. For the 100 nm and 60 nm gold
448 particles, we observed that their surface charges in the nanochannel were lower than obtained
449 from the zeta potential measured outside the nanochannel. Due to this deviation, we report the

more representative values of the surface charges measured in the nanochannel, which were obtained from scatter plots of the position of particles driven by electrophoresis along the nanochannel. To calculate the electric free energy from ion redistribution (F), the electrostatic and entropy-related energies from the charge distribution were integrated over the computational domain of the nanovalve[37]. The particle was moved through the constriction of the nanovalve to obtain $F(\mathbf{r})$, where $\mathbf{r}$ is the particle position. If the Debye length is sufficiently long (few tens of nm), $F(\mathbf{r})$ is modulated due to the topographical features in the nanovalve[37].

The potential energy U_P can be written as

$$U_P(\mathbf{r}) = F(\mathbf{r}) + z_p e\varphi(\mathbf{r}), \quad (4)$$

where z_p and φ are the number of elementary charges that the particle carries and the electric potential associated with the electric field $\mathbf{E}$ (induced by the electrodes), respectively. According to equation (4), an electric field induced externally by the nanoelectrodes bends the potential energy profile stemming from the charge distribution. To determine φ in steady state we use an equivalent electrical model for the charge transport in the electrolyte[39] and solve the following set of equations

$$\mathbf{J} = \sigma_m \mathbf{E}, \quad (5)$$

$$\nabla \mathbf{J} = 0, \quad (6)$$

$$\mathbf{E} = -\nabla\varphi, \quad (7)$$

where σ_m is the electrical conductivity of the electrolyte, and $\mathbf{J}$ is the electric current density. This set of equations was numerically solved in COMSOL Multiphysics for the specified geometry of the trap-in-channel system in a 50 μm long nanochannel (h = 300 nm, w = 500 nm)

471 (Supplementary Fig. 1). The boundary conditions have to account for the current-voltage relation
472 (Supplementary Fig. 9) of the electrodes at electrode boundaries ($\mathbf{n} \cdot \mathbf{J} = \mathrm{IV}\,(\varphi - \varphi_e)$), zero
473 normal current density at the channel walls ($\mathbf{n}\cdot\mathbf{J}=0$) and ground potential ($\varphi = 0$) at the two ends
474 of the nanochannel, which are connected to the μ-channels. Parameter σ_m can be modeled as the
475 sum of the bulk and the surface conductivities, and for the case of a monovalent electrolyte it
476 reads $\sigma_m \approx 2n_1 e\mu + 4|q_s|\frac{\mu}{h}$, where μ is the ion mobility[40] (electrolytes used in the DC mode are
477 monovalent). At ionic strength I = 0.05 mM (n_1 = 0.05 mM) we assumed $q_s \approx -1.0$ mC/m^2 for
478 the SiO_2 channel walls[37,38] and obtained $\sigma_m \approx 1.8$ mS/m .

479 The DC electric field $\mathbf{E}_{DC}$ in the nanovalve can trigger an osmotic flow and a viscous drag force
480 is exerted on the particle. The more rigorous electrokinetic analysis of our system using the
481 coupled equations of Poisson-Nernst-Planck (PNP) and Navier-Stokes (NS) shows that the
482 viscous drag force is sufficiently small compared to the electrostatic force so that the effect of
483 osmotic flow can be neglected (Supplementary Fig. 10). This analysis also shows that the model
484 employed in this manuscript to explain the particle position in the DC mode is in acceptable
485 agreement with the more precise potential energy function of the particle obtained using PNP
486 and NS (Supplementary Fig. 10).

487 <u>AC mode</u>

488 The AC mode is employed when the DC mode fails to generate topographically induced
489 potential energy barriers, i.e. for electrolyte ionic strengths I > ~0.5 mM and/or when the charge
490 densities on channel walls or particle surface are too low[9]. In the AC mode (also termed as
491 dielectrophoresis[24]), we exploit the difference in the polarizability of the particle and the

electrolyte to generate a restoring force (potential energy barrier) for the particle[24]. By spatial integration of the dielectrophoretic force equation, one obtains the potential energy function associated with this force for a sphere of radius *R* and permittivity ε_p^* immersed in an electrolyte ε_m^* in alternating excitation electric field with rms value $|\mathbf{E}_{AC}|$

$$\left\langle U_P(\mathbf{r}) \right\rangle = -2\pi\varepsilon_m R^3 \,\mathrm{Re}\left(\frac{\varepsilon_p^* - \varepsilon_m^*}{\varepsilon_p^* + 2\varepsilon_m^*} \right) \left| \mathbf{E}_{AC}(\mathbf{r}) \right|^2 . \qquad (8)$$

The starred quantities are the complex permittivites of medium (m) and particle (p) and the term $CM = \frac{\varepsilon_p^* - \varepsilon_m^*}{\varepsilon_p^* + 2\varepsilon_m^*}$ is referred to as Clausius-Mossotti factor. $\varepsilon^*_{p,m} = \varepsilon_{p,m} + i\sigma_{p,m}/\omega$ is the frequency-dependent complex permittivity, where ε, σ, and ω are the permittivity, conductivity and angular frequency, respectively. The real part of the *CM*-factor can attain values in the range between -0.5 to 1 for a spherically shaped particle and varies with frequency[18,24]. For negative values a potential energy barrier (potential energy maximum) is obtained at the constriction due to the topographically induced increase of the electric field, $\mathbf{E}_{AC}$, in this location. Equation (8) assumes that the material of the particle is homogenous and that the variations of $\mathbf{E}_{AC}$ across the particle are negligible[24]. The real part of the *CM*-factor of dielectric particles in solution with high ionic strength is typically negative and independent of the frequency ($\sigma_m > \sigma_p$ and $\varepsilon_m > \varepsilon_p$ [18,24]). For the biological and synthetic particles studied in our work in ionic concentrations ranging from 0.1X to 1X the observed *CM*-factor was safely in the negative region. In our analysis, we see immediately that the double layer interactions between particle and channel walls are negligible in the AC mode ($I > 0.5$ mM or channel wall passivation) and, hence, we do not consider the double layer interactions in the potential energy function for the AC-mode

512 (equation (8)). For simulating our experimental results, we also neglect the polarization of the
513 double layer of the particle in the electric excitation field $\mathbf{E}_{AC}$[41].

514 To determine $\mathbf{E}_{AC}$, we substitute the conductivity σ_m in equation (5) by the complex
515 conductivity $\sigma_m^* = \sigma_m + i\omega\varepsilon_m$ and solve the set of equations (5) - (7) in the frequency domain by
516 applying the boundary conditions $\mathbf{n} \cdot \mathbf{J} = j\omega C_e (\varphi - \varphi_e)$ and $\mathbf{n}\cdot\mathbf{J} = 0$ for the electrodes and
517 channel walls, respectively. Here φ_e and $C_e = 0.015$ F/m^2 are the electrode potential and the
518 equivalent specific electrode capacitance accounting for the 2-nm SiO_2 electrode insulation,
519 respectively. Ground potential ($\varphi = 0$) is used as boundary condition for the ends of the
520 nanochannels, which are connected on the chip to the μ-channels. The capacitance of the double
521 layer at the electrodes ($C_D > 0.12$ F/m^2 according equation 6 in reference [39]) is neglected since
522 the capacitance of the 2-nm SiO_2 electrode insulation ($C_e = 0.015$ F/m^2) is much lower for buffer
523 concentrations ≥ 0.1X. From the simulations, we observe that the formation of a double layer at
524 the electrodes is inhibited for the 0.1X ionic concentration and a partial layer ($(\varphi_e - \varphi) \approx$
525 $0.25 V_{AC}$) is formed for the 1X ionic concentration at the employed frequency f = 10 MHz. This
526 is because the characteristic relaxation time $\tau_c = \frac{\kappa^{-1} d}{D}$ (d: the electrode separation) is ≈ 0.6 μs
527 and ≈ 0.2 μs for 0.1X and 1X concentrations, respectively[39]. To reduce the formation of the
528 double layer at the electrodes the frequency of the applied AC voltage can be increased (our
529 experimental setup was limited to 10 MHz).

530 By inserting the equation (8) into the Boltzmann equation (equation (2)) we have

$$p(\mathbf{r}) = \frac{\exp\left(\dfrac{-2\pi\varepsilon_m R^3 \,\mathrm{Re}(CM)\left|\mathbf{E}_{AC}(\mathbf{r})\right|^2}{k_B T}\right)}{\dfrac{1}{V}\int_V \exp\left(\dfrac{-2\pi\varepsilon_m R^3 \,\mathrm{Re}(CM)\left|\mathbf{E}_{AC}(\mathbf{r})\right|^2}{k_B T}\right)|d\mathbf{r}|} \tag{9}$$

where $p(\mathbf{r})$ is the position probability density distribution, which we obtain experimentally, $\mathbf{E}_{AC}$ is obtained by FEM simulations as explained above, and we determine Re(*CM*) as a fitting parameter, which is calculated by equating the two sides of the above equation and employing a least-square curve fitting method.

Supplementary Fig. 11 shows the simulated potential energy and position probability distribution for a 100 nm sized particle (polystyrene bead) along a trap structure at a distance of 70 nm from the channel upper wall. By fitting the experimentally determined probability density to the probability density function obtained from simulation using the real part of the *CM*-factor as a fitting parameter, the effective real part of the *CM*-factor can be obtained. The experimentally determined probability density has to be corrected for the finite exposure time before the fitting (see section "Correction for Finite Exposure Time"). This effective real part of the *CM*-factor can be employed to update and, hence, increase the precision of the simulated potential energy profiles and the estimated potential energy barrier height.

With a simple analysis, the potential energy barrier in the AC mode can be approximately related to the characteristic cross-sectional dimension *L* of the channel constriction. For the condition that the channel length at the constriction (*s*) (Fig. 1a) is much smaller than the electrode separation distance (*d*), the complex electric current (electrical and displacement currents) flowing through the constriction remains approximately constant when the characteristic cross-sectional dimension *L* is varied (all other geometrical dimensions and ionic strength of the

551 solution are kept constant). This can be explained by the fact that the complex electric current
552 between the electrodes is determined by the complex electrical impedance between the
553 electrodes, which, assuming a negligible *s*, is almost independent of the characteristic cross-
554 sectional dimension *L*. Based on the analysis above it follows that $|\mathbf{J}_{AC}|^2$ is approximately
555 proportional to $1/L^4$ and, therefore, considering equation (5) with the complex conductivity
556 $\sigma_m^* = \sigma_m + i\omega\varepsilon_m$, $|\mathbf{E}_{AC}|^2$ almost scales with $1/L^4$.

557 The effects of joule heating and electrothermally induced fluid flow on the particle were found to
558 be negligible using COMSOL simulations (Supplementary Text and Supplementary Figures 12
559 and 13).

References for the Methods

30. Greber, U. F., Nakano, M. Y. & Suomalainen, M. Adenovirus Entry into Cells: A Quantitative Fluorescence Microscopy Approach. *Methods Mol. Med.* **21,** 217–230 (1998).

31. Fleischli, C. *et al.* Species B adenovirus serotypes 3, 7, 11 and 35 share similar binding sites on the membrane cofactor protein CD46 receptor. *J. Gen. Virol.* **88,** 2925–2934 (2007).

32. Nagel, H. *et al.* The alphavbeta5 integrin of hematopoietic and nonhematopoietic cells is a transduction receptor of RGD-4C fiber-modified adenoviruses. *Gene Ther.* **10,** 1643–1653 (2003).

33. Suomalainen, M. *et al.* A direct and versatile assay measuring membrane penetration of adenovirus in single cells. *J. Virol.* **87,** 12367–79 (2013).

34. Mojarad, N., Sandoghdar, V. & Krishnan, M. Measuring three-dimensional interaction potentials using optical interference. *Opt. Express* **21,** 9377–89 (2013).

35. Mojarad, N. & Krishnan, M. Measuring the size and charge of single nanoscale objects in solution using an electrostatic fluidic trap. *Nat. Nanotechnol.* **7,** 448–52 (2012).

36. Overbeek, T. The role of energy and entropy in the electric double layer. **51,** 61–75 (1990).

37. Krishnan, M. Electrostatic free energy for a confined nanoscale object in a fluid. *J. Chem. Phys.* **138,** 114906 (2013).

38. Behrens, S. H. & Grier, D. G. The charge of glass and silica surfaces. *J. Chem. Phys.* **115,**

6716–6721 (2001).

39. Bazant, M. Z., Thornton, K. & Ajdari, A. Diffuse-charge dynamics in electrochemical systems. *Phys. Rev. E - Stat. Nonlinear, Soft Matter Phys.* **70,** 1–24 (2004).

40. Stein, D., Maarten Kruithof & Dekker, C. Surface charge governed ion transport in nanofluidic channels. *Phys. Rev. Lett.* **4,** 137–142 (2004).

41. Shilov, V. N. *et al.* Polarization of the Electrical Double Layer. Time Evolution after Application of an Electric Field. *J. Colloid Interface Sci.* **232,** 141–148 (2000).

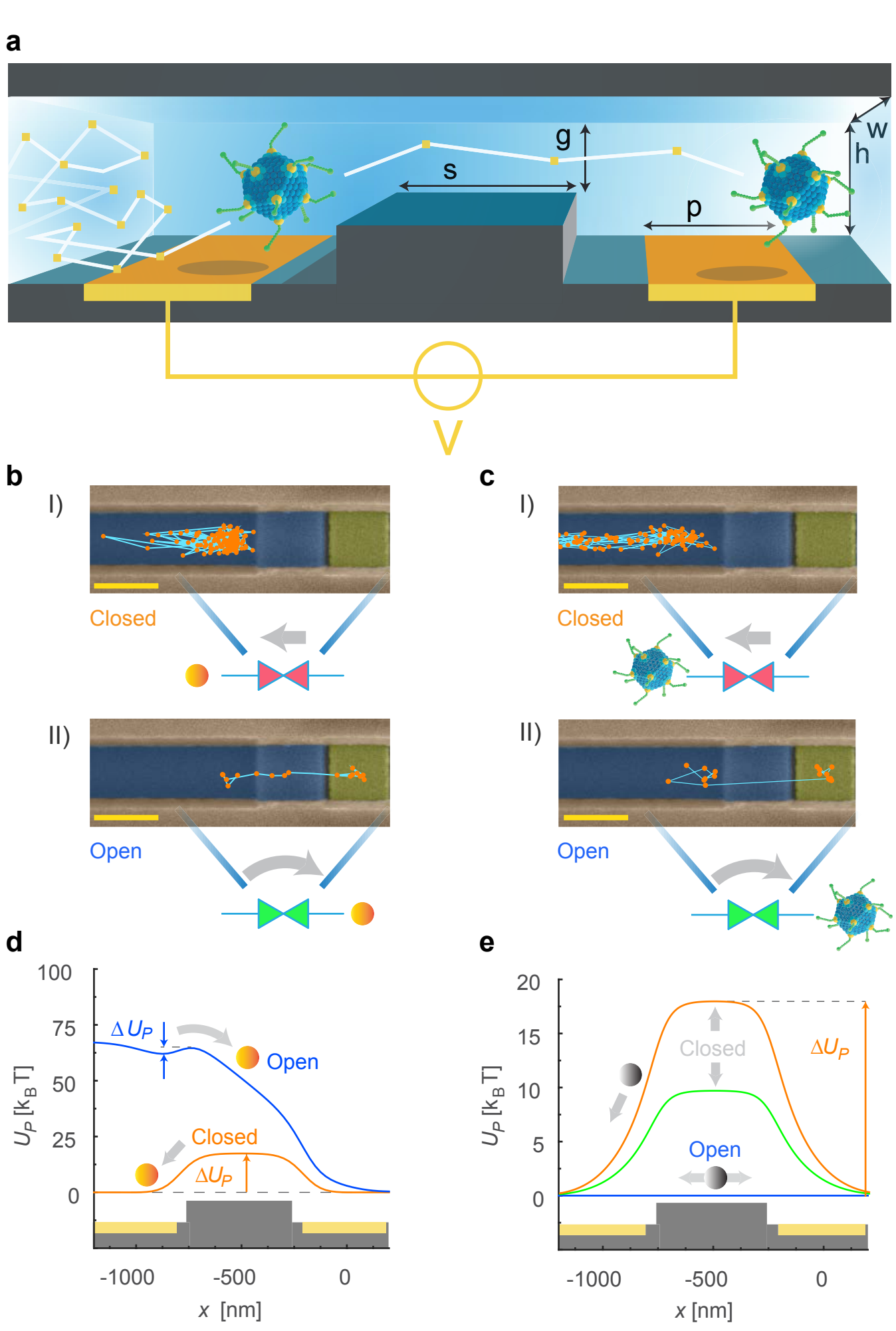
a
g
s
p
w
h
V
b
I)
Closed
II)
Open
c
I)
Closed
II)
Open
d
100
75
50
25
0
U_P [k_BT]
ΔU_P
Open
Closed
ΔU_P
-1000
-500
0
x [nm]
e
20
15
10
5
0
U_P [k_BT]
Closed
ΔU_P
Open
-1000
-500
0
x [nm]

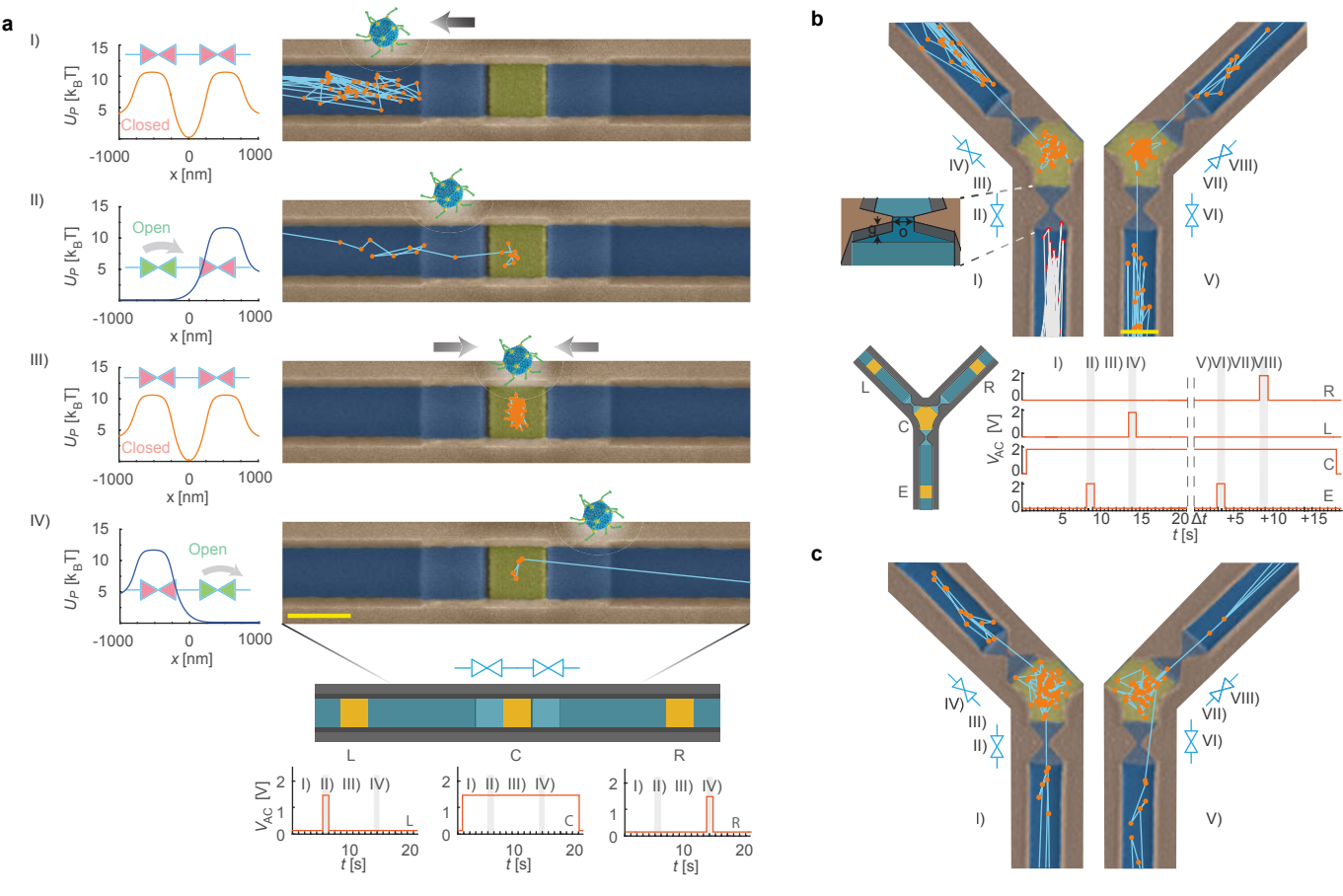
a
I)
II)
III)
IV)
U_P [k_BT]
x [nm]
Closed
Open
L
C
R
V_{AC} [V]
t [s]
b
I)
II)
III)
IV)
V)
VI)
VII)
VIII)
L
C
R
E
V_{AC} [V]
Δt
t [s]
c

a

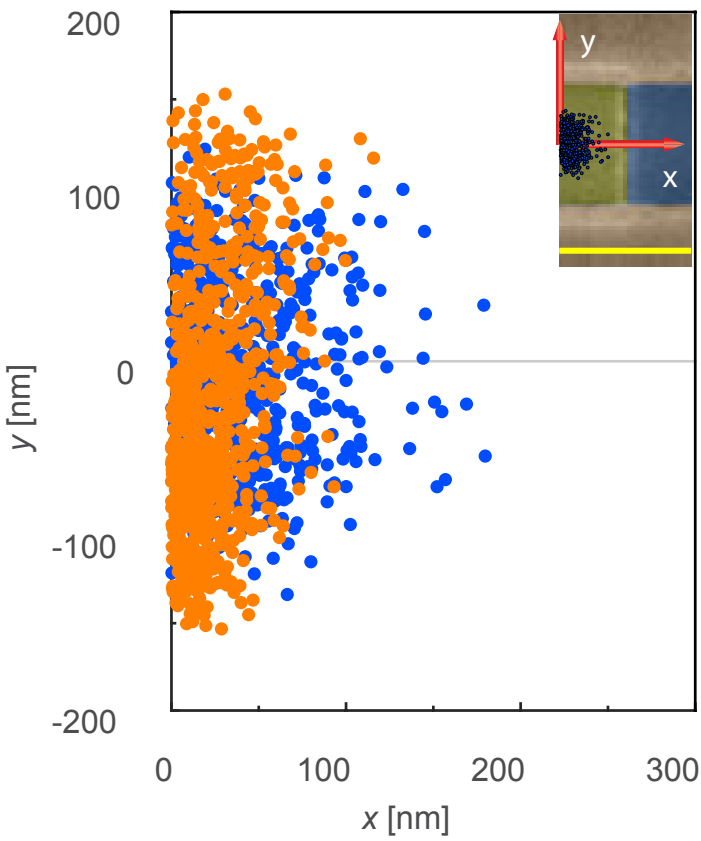
200
100
0
-100
-200
y [nm]
0
100
200
300
x [nm]
y
x

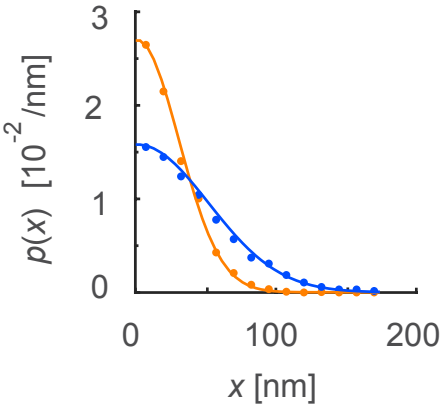
3
2
1
0
p(x) [10^-2 /nm]
0
100
200
x [nm]

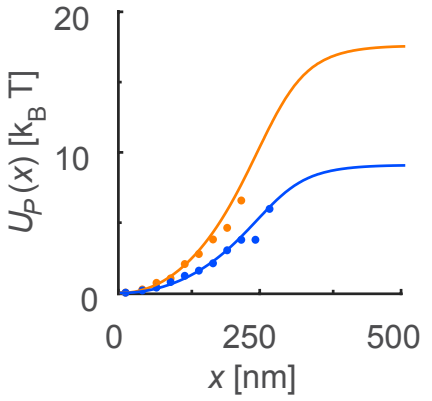
20
10
0
U_P(x) [k_B T]
0
250
500
x [nm]

b

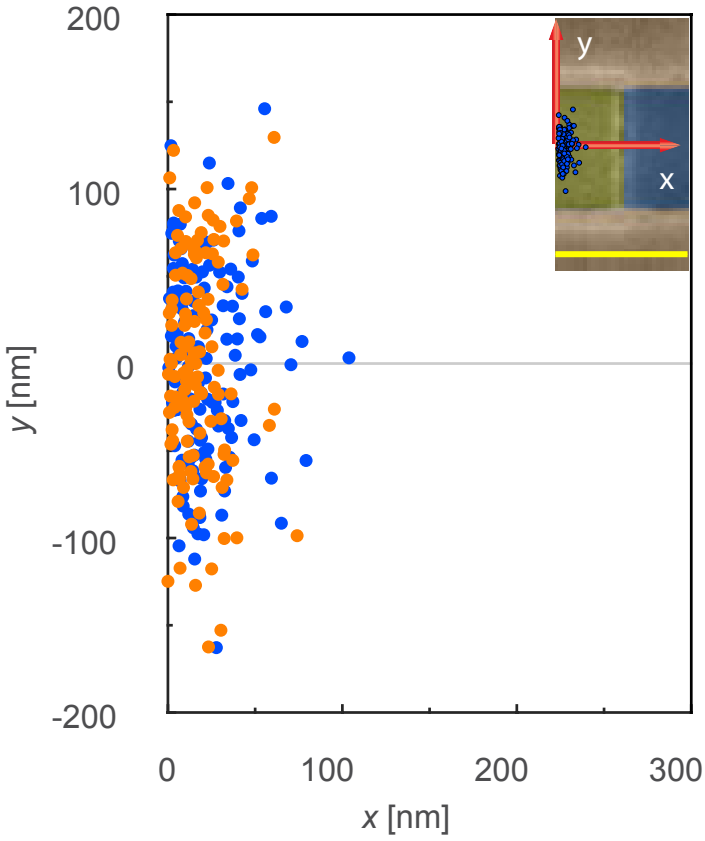
200
100
0
-100
-200
y [nm]
0
100
200
300
x [nm]
y
x

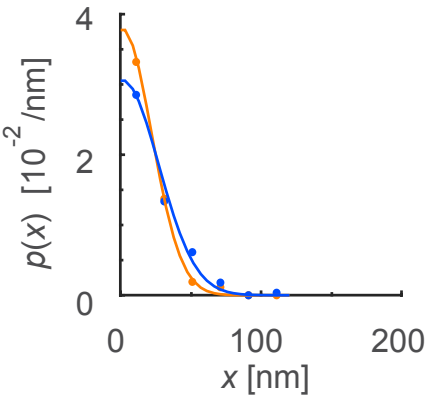
4
2
0
p(x) [10^-2 /nm]
0
100
200
x [nm]

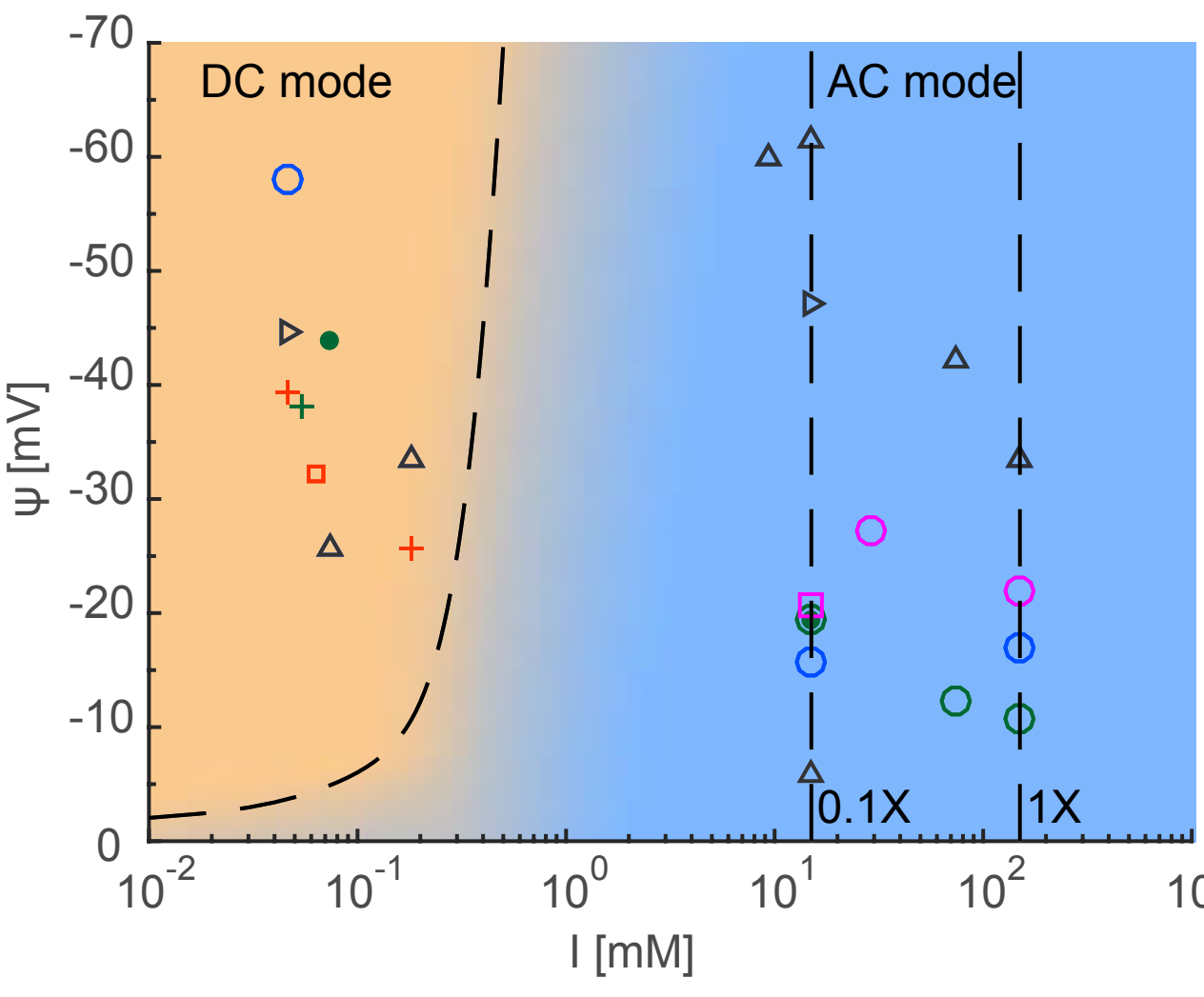

Particle Type	Size	Passiv.
Gold	100 nm	
Gold	60 nm	
Gold Rod	50x100 nm	
Polystyrene	100 nm	
Polystyrene	40 nm	
Lipid Vesicle	~100 nm	
Lipid Vesicle	~100 nm	(BSA)
Adenovirus	~90 nm	(PEG)
Quantum Dot	~10 nm	
Immunoglobulin G	~10 nm	(BSA)